PHYSICAL REVIEW B, VOLUME 63, 054524

^{4}He third-sound pulse collisions

M. P. Lilly,* F. Portier,† and R. B. Hallock
Laboratory for Low Temperature Physics, Department of Physics, University of Massachusetts, Amherst, Massachusetts 01003

(Received 14 July 2000; published 16 January 2001)

We investigate the behavior of pulses of ^{4}He third sound that propagate and collide on a glass substrate. Third sound is created by a thermal source and detected by evaporated metal superconducting transition-edge thermometers. Two thermal sources located symmetrically on either side of a detector allow third-sound pulses to be created, propagate through each other, and be detected. By varying the delay of the pulse launch between the two sources, the collision can be placed at an arbitrary position on the substrate. We present detailed observations of the evolution of the amplitudes of the third-sound pulses in collision. We also report measurements on the effect of the pulse collision on the propagation time of flight of the third-sound pulses. Experimental results for the time of flight change induced by the collisions are compared with quantitative expectations based on the two fluid model and a stronger effect is observed than expected.

DOI: 10.1103/PhysRevB.63.054524 PACS number(s): 67.40.Pm, 67.57.De, 67.40.Hf, 67.70.+n

I. INTRODUCTION

At low temperatures helium adsorbs uniformly to most substances and as the pressure inside a container is increased, the local film thickness increases in proportion to the changing chemical potential. For temperatures below 2.17 K ^{4}He films thicker than a few atomic layers are superfluid and support the propagation of waves called third sound. These film thickness fluctuations are analogous to tidal waves on the ocean, and have been studied in some detail over a number of years. First observed and described by Atkins and co-workers,[1,2] third sound waves involve a change in the local thickness and temperature of the film.[3] The use of superconducting transition-edge thermometers[4] accelerated the early understanding of many of the properties of third sound.[5] The study of third sound has provided insight into the properties of helium films,[6] including an enhanced understanding of the Kosterlitz-Thouless transition,[7,8] the behavior of persistent currents,[9] and the observation of a variety of nonlinear[10,11] and other effects.[12] In this work we confirm some of the nonlinear behavior of third sound when it is driven to saturation amplitudes [11] and then present a detailed study of the behavior of third-sound pulses in collision. Head-on collisions between third-sound pulses demonstrate that third-sound waves pass through each other and can be described by amplitude addition. In addition, a propagation time shift is introduced by the collision. This shift is compared to the predictions of a simple model and found to be larger than predicted.

II. EXPERIMENTAL DETAILS

A. Cryogenic environment

To provide a stable operating environment for our work we used a relatively standard cryostat insert and a continuously filling[13] 1 K refrigerator. A 78 cm^3 Cu sample chamber was attached to the 1 K platform with stainless steel posts and a weak thermal link (six Cu wires, 0.025 cm diam, 8.2 cm long). The sample chamber fill line attached to the sample chamber includes 30 cm of 0.43 mm I.D. stainless steel capillary at its cold end. This capillary was thermally anchored to the 1 K platform before reaching the sample chamber. When the sample chamber was empty, the six Cu wires provided the dominant heat leak. In the normal experimental situations, a superfluid ^{4}He film existed on the interior surfaces of the sample cell and the fill line, and the refluxing of the ^{4}He between the 1 K platform and the sample chamber along the fill line became the dominant heat leak. A sample chamber heater consisted of $\sim 250 \Omega$ (150 cm) of manganin wire wound in a bilayer wrap and varnished to the outside of the sample chamber. The weak thermal link between the 1 K platform and the sample chamber allows the sample chamber temperature to be controlled independently of the 1 K platform temperature and the temperature regulation could be set and controlled for several days without long-term drifts.

200 sheets of Nuclepore with 4000 Å diameter pores, were located inside the sample chamber to provide a film reservoir of ~ 4.9 m^2 and served to stabilize the chemical potential. Several thermometers were mounted on the sample chamber. One was a Ge thermometer calibrated over the range $0.3\,\mathrm{K} < T < 6.0\,\mathrm{K}$, accurate to ~ 1 mK. We calibrated a number of Allen-Bradley carbon composition resistors against the Ge thermometer. The secondary carbon resistors were used to regulate the temperature and to measure the changes in temperature. One was mounted in a Cu block and thermally attached to the bottom of the sample chamber; another was directly attached to the base of the sample chamber. A third was thermally connected to the top of the sample chamber and a fourth was attached to the 1 K platform. The experiments used an integrating feedback technique for temperature regulation. During the course of the various measurements the sample chamber temperature was raised 20 mK to 300 mK above the temperature of the 1 K platform, T_0, and held steady to a few tens of μK. This feedback technique worked best for temperatures near 1.5 K, where most of the experiments reported here were done.

B. Substrates and third-sound drivers and detectors

The third sound was propagated on a borosilicate glass substrate shown schematically in Fig. 1. The glass slide,

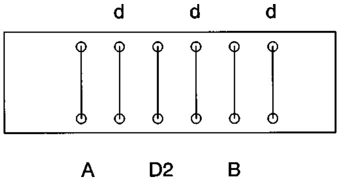

FIG. 1. Third-sound substrate design. *A* and *B* are Ag drivers and *D*2 is an Al transition edge thermometer. Three other Al electrode thermometers, *d* (not used in this work), were located on the substrate between *A* and *D*2, between *D*2 and *B*, and to the right of *B*. The electrodes are typically ~0.51 cm apart. Electrode $A(B)$ was located 1.056 (1.262) cm from the left (right) edge of the substrate. The distance between electrode $A(B)$ and *D*2 was 1.008 (0.998) cm. The right edge was roughened due to cutting the substrate to its final length. The uncertainty in the positions of the electrodes is ≈0.005 cm.

originally $2.54\,\mathrm{cm}\times 7.62\,\mathrm{cm}$, was shortened to $2.54\,\mathrm{cm}\times 4.3\,\mathrm{cm}$ by cutting one end with a glass cutter. The cut (right) edge of the glass slide was roughened ~0.012 cm by the cutting process. The third-sound Ag thermal drivers and Al detector thermometers were deposited by thermal evaporation. A plasma ion etch (1.5 kV at 0.05 Torr of air for 15 min) was performed in the evaporation chamber immediately before the evaporation to clean the glass surface and enhance the adherance of the deposited metals. In three separate evaporations, 100 nm thick Ag pads were evaporated, and then two Ag drivers ($1.91\,\mathrm{cm}\times 0.013\,\mathrm{cm}\times 30\,\mathrm{nm}$) labeled *A* and *B* in Fig. 1 and four Al themometers (detectors) ($1.91\,\mathrm{cm}\times 0.013\,\mathrm{cm}\times 30\,\mathrm{nm}$) were deposited. In this experiment, only the two drivers (*A* and *B*) and a single detector ($D2$) were used. The distance between *D*2 and driver $A(B)$ was 1.008 (0.998) cm. The configuration is shown in Fig. 1. The ends of the Al thermometers covered half of the Ag pads, leaving the other half of the Ag exposed and Cu leads (0.004 in diam) were attached using indium solder. The driver resistance values were $R_A = 112\,\Omega$ and $R_B = 135\,\Omega$ under experimental operating conditions. The detector (thermometer) was biased at its superconducting transition with a dc bias current. For a typical bias current of 70.2 μA, the calibration of the resistance as a function of temperature in the operating range of the experiments ($T \approx 1.45\,\mathrm{K}$) resulted in a detector sensitivity $\delta R/\delta T = 823\,\Omega/\mathrm{K} = s$.

C. Electronics for pulsed third sound

Third sound pulses were created using two Stanford Reseach Systems DS 345 pulse generators to apply a voltage for a short time across the resistance of the selected Ag driver, *A* or *B*. The energy deposited in the driver caused local heating and created the third sound. Most of the experiments were performed with square-wave drive pulses with a zero volt baseline, a voltage amplitude *V* and a width (duration) *W*. The function generators were configured in the *burst* mode, where on receipt of a trigger pulse a delayed square pulse was launched. With two function generators, these delayed square pulses could have different width, delay, δ, and amplitude parameters for each of the drivers: W_A, δ_A, V_A, W_B, δ_B, and V_B. The range the square-wave pulse amplitudes was $0.3 \leqslant V_i \leqslant 2$ V and the range of the pulse widths was $40 \leqslant W_i \leqslant 600\,\mu\mathrm{sec}$, resulting in drive pulse energy values $E_i = V_i^2 W_i / R_i$ in the range $30\,\mathrm{nJ} \leqslant E_i \leqslant 20\,\mu\mathrm{J}$. The range of the delay that could be introduced was $0 \leqslant \delta_i \leqslant 2000\,\mu\mathrm{sec}$.

Temperature fluctuations caused by the third sound pulses were detected by the change in the resistance of the Al thermometer (detector) *D*2. For the thermometer used in this work the useful temperature range with no applied magnetic field was typically 1.4 K to 1.6 K. The dc bias current resulted in a voltage fluctuation across the detector due to the passage of a third sound pulse and this was amplified by an Ithaco 1201 low noise preamplifier with a gain of 1000, notched to pass frequencies in the range $30\,\mathrm{Hz} < f < 100\,\mathrm{kHz}$. The amplified signal was digitized by a DSP 2030S, an 8-bit digitizer that sampled the signal every 1.33 μsec. Digitizing began on the receipt of the trigger (no pretrigger). The trigger (i.e., drive pulse) frequency was 23 Hz and the source was the trigger output of one of the SRS DS 345 function generators. The number of digitized voltage samples in a single third-sound pulse measurement data set was typically 2048, for a total signal duration of 2724 μsec. The digitized data set was transferred to a DSP 4100 (the averaging memory) and after 1000 such data sets the averaged data set (a signal-averaged third-sound pulse signature) was transferred to a computer for storage and analysis. One of the relevant parameters was then changed and the process repeated.

All of the electronics was synchronized by the computer, which could turn on and off each of the drivers and set each of the six parameters that characterized the delayed square pulses created at driver *A* and driver *B*. With this capability, the computer could be programmed to automatically record third sound pulses for a range of amplitudes and pulse launch delays.

III. SINGLE THIRD-SOUND PULSE MEASUREMENTS

In this section we describe some single-pulse third-sound characteristics prior to discussing the collision experiments. The general features of a typical third-sound pulse at $T = 1.453\,\mathrm{K}$ for $d = 6.0$ layers are shown in Fig. 2. This pulse was generated at driver *A* with $V_A^2 = 0.3(\mathrm{volts})^2$, $W_A = 200\,\mu\mathrm{sec}$ and $\delta_A = 0\,\mu\mathrm{sec}$. For $R_A = 112\,\Omega$, $E = 0.54\,\mu\mathrm{J}$ for the drive pulse which produced the third-sound pulse shown in Fig. 2. Only a small fraction of this energy is carried in the third-sound pulse,[11] the rest is lost to the substrate, evaporation, etc. At $t = 0\,\mu\mathrm{sec}$ and $t = 200\,\mu\mathrm{sec}$, the sharp spikes are the pickup signals from the square-wave voltage steps on the driver. These pickup pulses always occurred when square pulses were used for initiating a third-sound pulse and although they are parasitic signals, they provide a very useful *in situ* confirmation directly in the data sets of the duration (width) of the thermal drive pulse. After the pickup pulse, the amplitude becomes flat and we use this region as a signal strength, δV, baseline to define $\delta V = 0$. At $t \approx 500\,\mu\mathrm{sec}$, the leading edge of the third-sound pulse

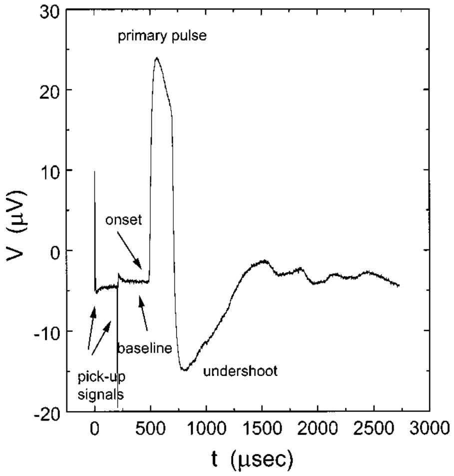

FIG. 2. Third-sound pulse with a driver amplitude of $V_A^2 = 0.3\,(\mathrm{volts})^2$ (unsaturated) and $W_A = 200\,\mu\mathrm{sec}$ at $T = 1.453\,\mathrm{K}$ and $d = 6.0$ layers. Various features of the pulse such as the primary pulse, the undershoot and the pickup pulses are noted.

arrives at the detector. The *primary pulse* is the warm and thin region of the third-sound wave. Following the primary pulse, we observe an *undershoot*, a cool and thick region. The features of the primary pulse and the undershoot evolve as a function of drive voltage, drive width, temperature and film thickness.[11]

A. The third-sound temperature wave

The raw data was in the form of voltage measurements, but these voltage changes were the direct result of resistance changes in the thermometer caused by temperature changes due to the third-sound pulses. Since the voltage measurement recorded by the digitizer used an arbitrary $V = 0$ value, as noted, we shifted[14] each data set so that the baseline was normalized to $\delta V = 0$. The shifted data sets were used to calculate the temperature fluctuations, to calculate times of flight, etc. In Fig. 3 we show an example. The raw data from the digitizer is in Fig. 3(a). The baseline was determined by using data in the time span $300\,\mu\mathrm{sec} < 420\,\mu\mathrm{sec}$ and $\delta V(t)$ is shown in Fig. 3(b). The temperature swing δT corresponding to the δV in Fig. 3(b) was found using the thermometer sensitivity, $s = 823\,\Omega/\mathrm{K}$ and the bias current, $I_{\mathrm{bias}} = 70.2\,\mu\mathrm{A}$, $\delta T = \delta V / s I_{\mathrm{bias}}$. The $\delta T(t)$ results are shown in Fig. 3(c). We will return to Fig. 3(d) later.

B. Single-pulse time of flight

Given the large number of data sets to be recorded during the course of this work and our desire to document the effect of third-sound pulse collisions on third sound times of flight, an automatic technique for the time of flight determination was essential. This was accomplished as follows. Using the baseline-shifted data set, we fit a line to the initial rise of the primary pulse, and the time where this line crosses $\delta V = 0$ defines the arrival time, Γ, of the pulse. Γ is the time interval between the trigger pulse (which defines $t = 0$) and the arrival time of the leading edge of the primary pulse. We use Fig. 4 to illustrate the method of third-sound arrival time determination. First, the raw data, $V(t)$, was offset to shift the baseline to $\delta V = 0$. In Fig. 4(a), the offset data set, $\delta V(t)$, is shown with a line added at $\delta V = 0$ to emphasize the baseline. In order to determine the onset of the third-sound pulse, we used a linear fit to 17 data points (22.7 μsec) located along the rapidly rising leading edge of the primary pulse. The center point of this range of 17 points was defined to be the maximum of the derivative of $\delta V(t)$ with respect to time. This derivative is shown in Fig. 4(c). For the specific case shown here, the maximum of the derivative occurred at $t = 501.2\,\mu\mathrm{sec}$, and the range of the linear fit was $490.5\,\mu\mathrm{sec} \leqslant t \leqslant 511.9\,\mu\mathrm{sec}$. This range is defined in Figs. 4(b) and 4(c) with dashed vertical lines. A fit to $\delta V(t)$ in this region results in a line that fits the leading edge of the primary pulse, which is plotted in both 4(a) and 4(b). The intersection of this line with $\delta V = 0\ \mu$ sec defined the arrival time, $\Gamma = 490.9\,\mu\mathrm{sec}$. This procedure was automated to allow calculation of the times of flight for a large number of pulses using a consistent method. In general the time of flight, τ, is defined as the time between generating the pulse at a driver and detecting the pulse at the thermometer, $\tau = \Gamma - \delta$, where δ is the delay in the launch of the drive pulse that might be introduced after the trigger.

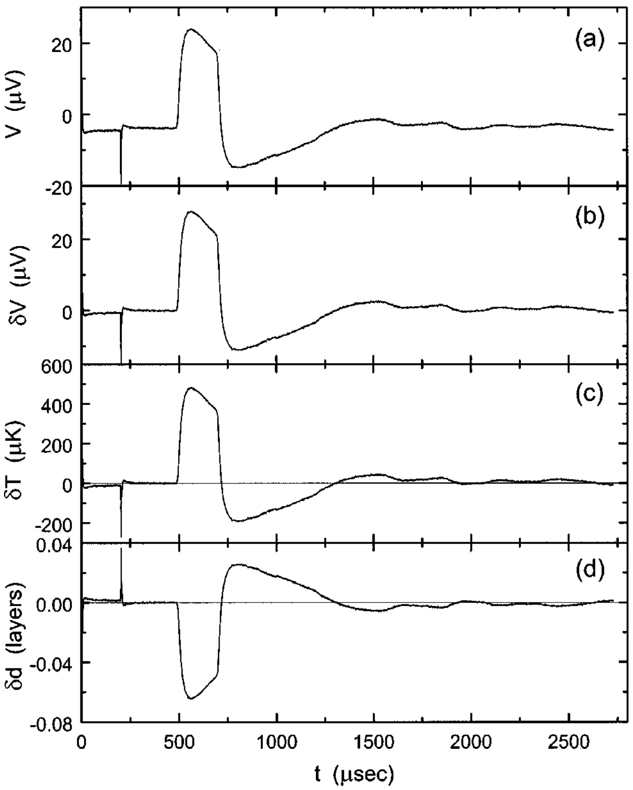

FIG. 3. Example of the calculation of δV, δT, and δd for a third-sound trace with $V_A^2 = 0.3\,(\mathrm{volts})^2$, $W = 200\,\mu\mathrm{sec}$, $T = 1.435\,\mathrm{K}$, and $d = 6.0$ layers. In (a) the raw data is shown. In (b), δV was normalized using a region $300\,\mu\mathrm{sec} \leqslant t \leqslant 420\,\mu\mathrm{sec}$ as the baseline. In (c) the temperature excursion was calculated from the calibrated transition-edge thermometer. In (d) we show the calculated thickness change using Eq. (5).

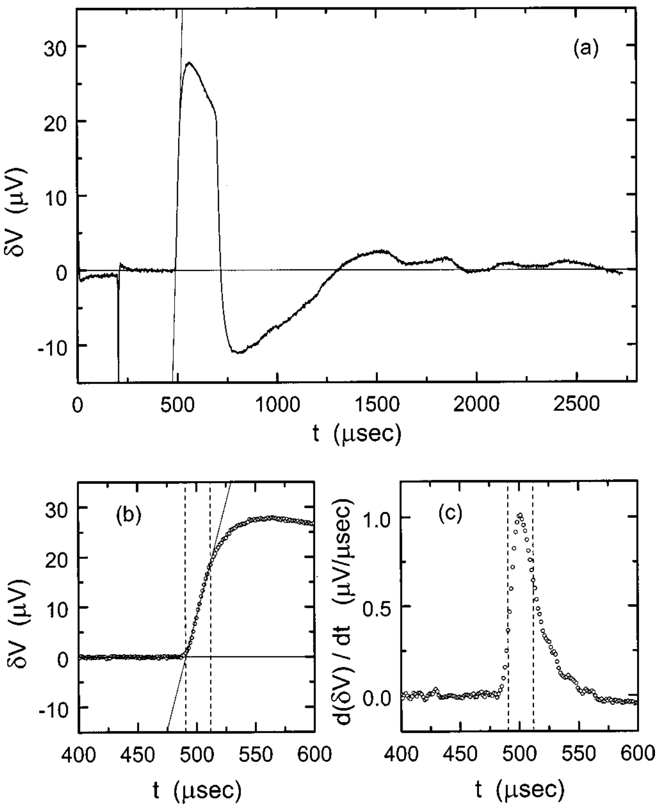

FIG. 4. Calculation of the third-sound arrival time for application of a square pulse, $V_A^2 = 0.3\,(\text{volts})^2$ and $W_A = 200\,\mu\text{sec}$, to driver A at $T = 1.453\,\text{K}$ and $d = 6.0$ layers. In (a), the entire trace, with the baseline offset to $\delta V = 0$, is shown. The intersection of the lines defines the time of flight. In (b), a closer view of the primary pulse is shown. The intersection of the two straight lines determines the time of flight. In (c), the maximum value of the derivative of $\delta V(t)$ is used to determine the range of data used to determine the leading-edge fitted line in (a) and (b) (see text).

C. Approximate thickness scale

The time of flight measurements for the single pulses were used to determine the approximate helium film thickness. Atkins[1,5] showed that the third-sound velocity is given by

$$C_3^2 \approx \frac{\rho_s}{\rho}\left(1+\frac{TS}{L}\right) f d, \tag{1}$$

where C_3 is the velocity, $f \simeq 3k_B\alpha/m_4 d^4$ is the restoring force per unit mass, α is the strength of the Van der Waals constant and d is the film thickness. The first factor, ρ_s/ρ, is the superfluid fraction and arises because only the superfluid moves when third sound propagates. The superfluid fraction is modified by the presence of the substrate, and we will correct for the effective value of the superfluid fraction shortly. The second term is due to evaporation and condensation effects, where S is the entropy per unit mass and L is the latent heat of evaporation per unit mass. A more complete exression for the restoring force, valid to larger film thickness values is given by[15]

$$f = \frac{1}{m_4}\left(\frac{\partial \mu}{\partial d}\right)_T = \frac{\alpha\beta(3\beta+4d)}{d^4(d+\beta)}\,\frac{k_B}{m_4}. \tag{2}$$

Here k_B is the Boltzmann constant and m_4 is the mass of a ^{4}He atom. A more detailed theoretical description of third sound was presented by Bergman,[6] in which the ^{4}He film, the ^{4}He vapor and the substrate were explicitly taken into account. He found the third-sound velocity to be

$$C_3^2 = \left\langle\frac{\rho_s}{\rho}\right\rangle\left(1+\frac{TS}{L}\right)^2 \frac{\alpha\beta(3\beta+4d)}{d^3(d+\beta)^2}\,\frac{k_B}{m_4}. \tag{3}$$

For a glass substrate,[15] $\alpha \approx 27$ layers ^{3}K and $\beta \approx 41.7$ layers. One difference from the velocity expression found by Atkins [Eq. (1)] is the quadratic dependence of the $(1+TS/L)$ term, which correctly accounts for evaporation and condensation between the film and the vapor. The presence of this quadratic dependence was confirmed experimentally by Galkiewicz *et al.*[16] A second difference is the explicit presence of the effective superfluid density, $\langle\rho_s/\rho\rangle$ in place of the bulk superfluid density. This incorporates the fact that for a helium film on an ordinary substrate (i.e., one that is not a weak-binding substrate) the superfluid density is depleted from the bulk value by the strong Van der Waals force very near to the substrate. For the thickness and temperature range of this experiment, an empirical expression provides values for $\langle\rho_s/\rho\rangle$. $\langle\rho_s/\rho\rangle = (\rho_s/\rho)(1-D/d)$ where[4] $D = a + bT(\rho/\rho_s)$. For a glass substrate,[15] $a \approx 0.5$ layers and $b \approx 1.13$ layers/K. The thickness of one ^{4}He layer is taken as 0.36 nm.

For our purposes we will take the third-sound velocity to have the Bergman form

$$\left(\frac{\Delta x}{\tau}\right)^2 = \left\langle\frac{\rho_s}{\rho}\right\rangle\left(1+\frac{TS}{L}\right)^2 \frac{\alpha\beta(3\beta+4d)}{d^3(d+\beta)^2}\,\frac{k_B}{m_4}, \tag{4}$$

where Δx is the measured propagation distance and τ is the measured time of flight. Using measured values for τ, the only unknown is the film thickness, d, and by numerically inverting Eq. (4) d can be determined. This procedure is known to give a reasonably accurate value for the film thickness for chemical potential values in the range used in this experiment. For the pulse in Fig. 4, $\tau_A = 490.9\,\mu\text{sec}$, $\Delta x_A = 1.008\,\text{cm}$ and numerical inversion of Eq. (4) results in $d = 5.90$ layers.

Since there were two third-sound drivers, we could compare the film thickness calculated by use of a pulse from driver A and a subsequent separate pulse from driver B. Using the same procedure as described earlier for the same conditions as in the figure, we found, $\tau_B = 513.2\,\mu\text{sec}$, and the thickness calculation with $\Delta x_B = 0.998\,\text{cm}$ resulted in $d = 6.17$ layers, somewhat different from the value of 5.90 layers determined for the pulse from driver A. We explore this difference in some detail in Appendix A. This modest inconsistency does cause an uncertainty in our determination of the superfluid film thickness and the film thickness is simply defined to be the average of d calculated for the pulses from the two drivers. As the work we report here is not very sensitive to the absolute film thickness and no studies were done that required a precise value for the film thickness, this averaging was considered acceptable.

D. Amplitude of the film thickness wave

The thermometer technique used to record third-sound pulses directly measured the temperature fluctuation of the pulse. In third sound, both the temperature and the film thickness oscillate. In order to obtain an estimate for the film thickness oscillation, $\delta d(t)$, that accompanied the temperature oscillation, $\delta T(t)$, we use the temperature-thickness relation predicted by Bergman[6]

$$\frac{\delta T}{T} = -\frac{df}{L}\frac{\delta d}{d}, \tag{5}$$

where f is the restoring force given by Eq. (2). In Fig. 3(d), we show an example of the calculated film thickness fluctuation, δd, for a third-sound pulse at $T = 1.453\,\mathrm{K}$ and $d = 6.0$ layers. For this example, using the Van der Waals constants for glass the film thickness fluctuation was computed to be $\delta d(\mathrm{layers}) = -1.34\times 10^2\,\delta T\,(\mathrm{K})$.

Brooks *et al.*[17,18] directly measured both the temperature change (with a superconducting transition-edge thermometer) and the film thickness change (with a capacitor) of pulsed third sound for a range of film thickness values. They found that the measured ratio of $\delta T/\delta d$ was frequency dependent and about a factor of two larger than predicted by Bergman[6] for the ^{4}He coverage range that we used in this work. Later measurements by Laheurte *et al.*[19] were consistent with those of Brooks *et al.*,[17,18] and found that consistency with the prediction of Bergman depended on temperature.[20] Calculating the thickness change from a given measured change in the temperature[21] is not the ideal method for finding the thickness change of the third sound pulse, but it is a reasonable approximation. Since we will be primarily interested in arrival times and the evolution of pulse shapes, and not explicit amplitude values, this does not represent a problem for us.

E. Saturation measurements

The features of third-sound pulses evolve with increasing drive amplitude. To properly prepare for the third-sound collision experiments it was necessary to study the behavior of single third-sound pulses on this substrate. In Fig. 5, we show a number of third-sound pulses from driver B at $T = 1.453\,\mathrm{K}$ and $d = 6.0$ layers that confirm the general behavior seen earlier by Wang *et al.*[11] In (a) a sequence of data sets for $\delta V(t)$ are stacked on top of one another. The smallest pulse corresponded to a drive energy of 0.148 μJ and the largest pulse shown here had a drive energy of 1.48 μJ. These pulses were taken with uniform increases in the square of the drive voltage, so each drive pulse is a constant 0.148 μJ greater in energy than the preceeding pulse. Examining Fig. 5(a), we see that the first four pulses had an increasing amplitude and a fixed width. For the fifth pulse the amplitude is saturated and the pulse is wider. After the fifth pulse, the remaining five pulses had about the same amplitude and increasing widths. The maximum amplitude as a function of drive energy is shown in Fig. 5(b). For $E \lesssim 0.7\,\mu\mathrm{J}, \delta V_{\max}$ increased linearly with amplitude. For $E > 0.7\,\mu\mathrm{J}$, the amplitude saturated. In Fig. 5(c), the width is shown as a function of the drive energy. In the linear region where $E \lesssim 0.7\,\mu\mathrm{J}$, the width remains at a fixed width of ~ 225 μsec, slightly above (due to time constant effects) the drive pulse width of 200 μsec. For convenience in the present context, the width W is defined[22] to be the time interval between the arrival of the leading edge of the primary pulse and the next crossing of the $\delta V = 0$ baseline. In the saturated region, the width grows linearly with increasing drive energy, consistent with more extensive earlier observations.[11]

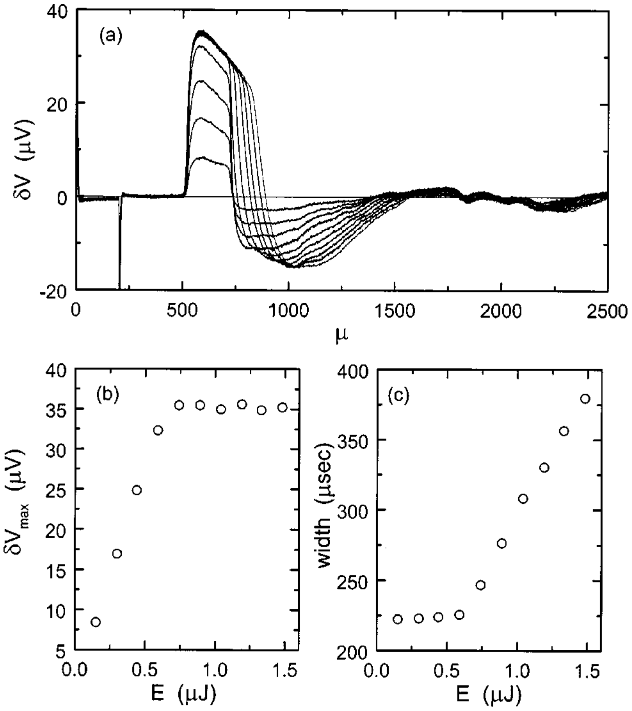

FIG. 5. Ten third-sound pulses from driver B with amplitudes ranging from 0.148 μJ to 1.48 μJ at $T = 1.453\,\mathrm{K}$ and $d = 6.0$ layers. In (a), the offset traces, $\delta V(t)$ are shown. In (b), the maximum δV of the primary pulse is shown as a function of drive energy. In (c) the width of the pulse is shown as a function of drive energy. Third-sound pulse amplitude saturation occurs at $E_{\mathrm{sat}} \approx 0.7\,\mu\mathrm{J}$.

The saturation of thermally generated third-sound pulses is believed to occur as a result of the events associated with the creation of the pulse at the third-sound driver.[11,23] When voltage is applied to the resistive Ag driver, the current pulse causes the driver to heat up and atoms are evaporated from the ^{4}He film. The removal of atoms from the film and local $\delta T > 0$ cause superfluid to flow toward the driver from opposite directions, creating the third-sound pulse. When the voltage is turned off, the inertia of the flow continues for a short time, causing an excess of helium at the driver and the consequent undershoot observed in the third-sound pulse following receipt of the primary pulse. If the amount of heat applied to the driver is high, the superfluid film reaches the critical velocity and the flow of atoms to the driver is limited with the result that evaporation cannot dissipate all of the

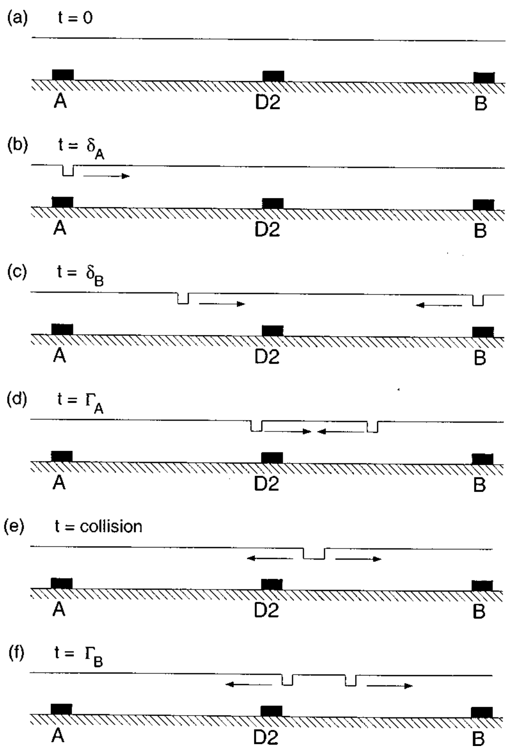

FIG. 6. Schematic drawing (not to scale) for $\delta_A < \delta_B$. In this case, the pulse from *A* arrives at the detector before being involved in a collision. Γ_i is the time the leading edge of the primary third-sound pulse from driver *i* arrives at detector *D*2.

thermal energy. The amplitude of the pulse cannot be increased further and it saturates. The extra energy goes into heating the substrate, so that when the drive pulse is turned off, the overheated substrate continues to draw superfluid, and the resulting third-sound pulse is wider than the applied square-wave drive. Ketola *et al.*[23] and Wang *et al.*[11] accounted for third sound attenuation and showed that the critical velocity deduced from third-sound pulse saturation measurements was generally consistent with measurements of the critical velocity carried out by other techniques. Given the extensive earlier work[11] on the behavior of third sound as a function of drive amplitude and width, we limited our observations to characterization of the third-sound available from each driver, noting the saturation points, and we did not explore these saturation effects further.

However, to prepare fully for the pulse collision experiments, in addition to measuring the amplitude and width of the third-sound pulses as a function of drive power, we also measured the time of flight of the pulses from driver *A* and driver *B* to determine if there was a drive amplitude dependence to our time of flight measurements. The results for pulses with $W = 200\,\mu$sec, $\delta = 0\ \mu$sec and $0.1 \leqslant V^2 \leqslant 4.0$ for both drivers are independent of drive amplitude to within $\pm 2\mu$sec (out of times of flight $\sim 500\ \mu$sec) over the full range of drive amplitude with systematic deviations within these limits. The time of flight deviations were a rather weak decreasing function of increasing drive amplitude for amplitudes below the saturation amplitude, and were more nearly independent of amplitude for pulses above the saturation value of $V^2 \approx 0.5\,(\text{volts})^2$. The generally correlated behavior for the two data sets from the two drivers suggests that the small systematic deviations are likely caused by small chemical potential drifts in the sample chamber during the course of the measurements. Similar behavior was observed for other values of *W*.

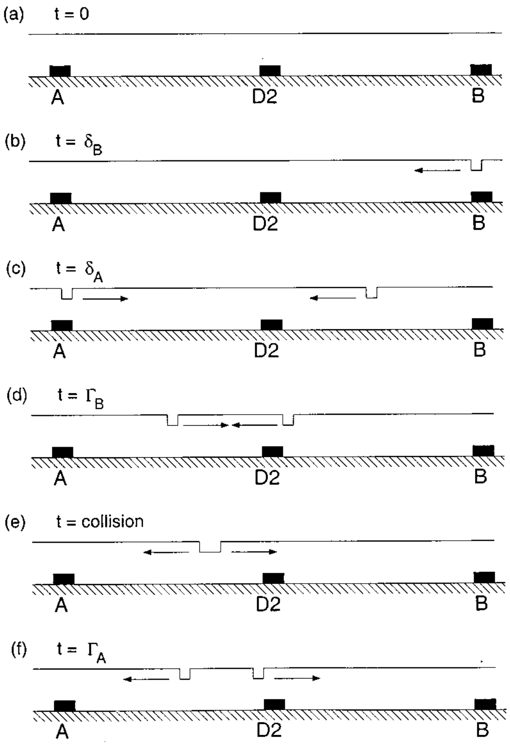

FIG. 7. Schematic drawing (not to scale) for $\delta_B < \delta_A$. In this case, the pulse from *A* arrives at the detector after being involved in a collision.

IV. HEAD-ON THIRD-SOUND PULSE COLLISIONS

With the foregoing discussion of single pulses, we now proceed to discuss the results of experiments involving head-on third-sound pulse collisions. Observations of collisions in an experiment of this type were reported previously by Ketola *et al.*[24] and a preliminary report from this experiment appeared earlier.[25] Our measurements of the effect of the collision event on the propagation time of third sound pulses were more accurate than the earlier measurements of Ketola *et al.*[24] because here we included simultaneous corresponding single pulse (noncollision) measurements. This enabled us to observe and document shifts in the time of flight of a free pulse vs one that had endured a collision. In the subsections that follow we will describe the technique for controlling the position of the collision on the substrate, study the detailed evolution of third sound pulse shapes during a collision, and we will examine the effect of a collision on the third-sound time of flight. We will find that a collision shifts the arrival time of a pulse. The features of the shift will be examined for collisions occurring at different positions relative to the detector and the maximum shift will be compared to a model calculation.

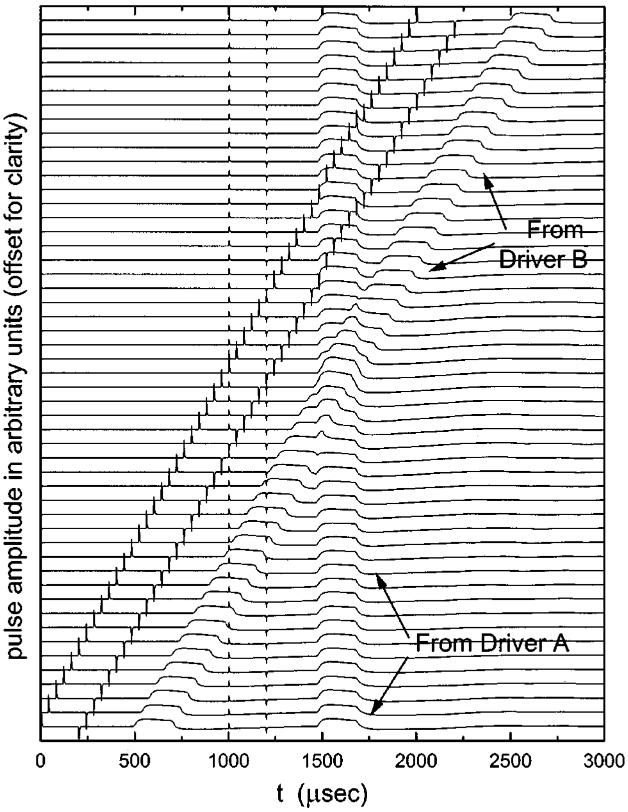

FIG. 8. Waterfall plot of a collision event with $W_A = W_B = 200\,\mu$sec and $V_A^2 = V_B^2 = 0.3\,(\text{volts})^2$ at $T = 1.453$ K and $d = 5.9$ layers. The delay for the pulse from A is fixed at $\delta_A = 1000\,\mu$sec, and the delay for the pulse from B is swept from $\delta_B = 0\,\mu$sec (bottom trace) to $\delta_B = 2000\,\mu$sec (top trace) in steps of 40 μsec. The pulse received at $\tau = 1473\,\mu$sec is the pulse from driver A in each case.

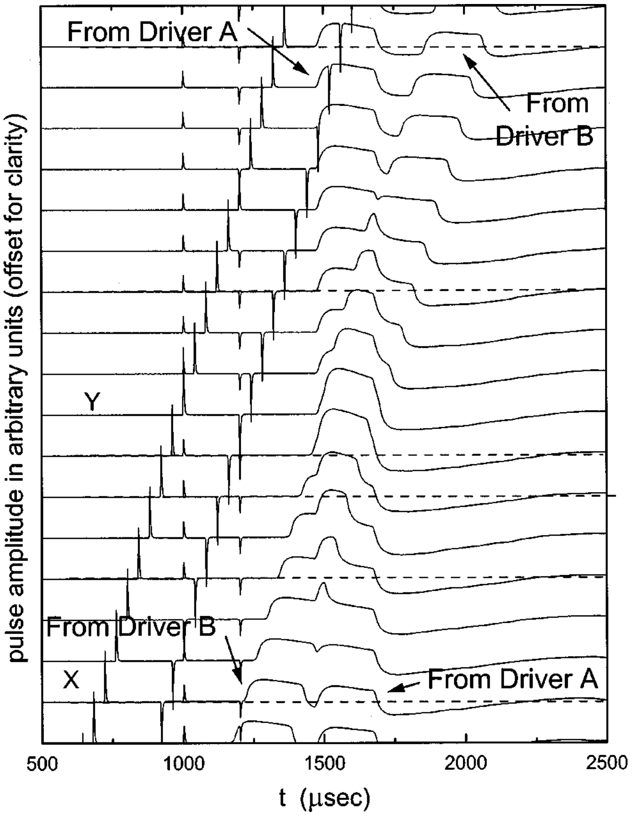

FIG. 9. Expanded waterfall plot of a collision event with $W_A = W_B = 200\,\mu$sec and $V_A^2 = V_B^2 = 0.3\,(\text{volts})^2$ at $T = 1.453$ K and $d = 5.9$ layers shown in Fig. 8. The change in the delay δ_B of the pulse from B from one data set to the next is 40 μsec.

A. Arranging a collision: the delay technique

One way to measure the effect of a collision would be to use many transition-edge thermometers between the driver and detector and record the effect of an evolving collision in the center of the substrate using all of the thermometers simultaneously. Because of the limited number of available leads to the sample chamber, we chose to use only one detector thermometer ($D2$) and we caused the collision to occur in different positions relative to the single thermometer by use of a sequence of collision events. In order to do this, we utilized the ability to control δ, the tunable delay of the square drive pulse relative to the trigger. In all of our experiments $\delta_A > 0$ was fixed for convenience and pulses were recorded for a range of δ_B values. We illustrate this technique for two cases, $\delta_A < \delta_B$ and $\delta_B < \delta_A$, and we show the important events in the schematic drawings in Fig. 6 and Fig. 7. The drivers (A and B, on either end) and the thermometer ($D2$, in the middle) are represented by black rectangles. The drawings are not to scale; the film thickness is not really dramatically reduced above an inactive driver or detectors, and the third sound pulses are of much larger spatial extent (~0.4 cm) than the width (~0.013 cm) of the drivers and the detector,[26] etc. We first treat the case $\delta_A < \delta_B$ (Fig. 6). At $t = 0$ the trigger occurs, but since $\delta_B > \delta_A > 0$ no pulses have been initiated yet. In Fig. 6(b), at $t = \delta_A$, a pulse is created at A traveling toward the detector. The pulse is wider[26] than shown in the figure. A pulse travels in the other direction as well, but this propagates away from the detector and has no effect on the detector in the time frame that we examine. At $t = \delta_B$ [Fig. 6(c)], a pulse is created at driver B. In this figure, the pulse from A has not yet reached the detector (but if δ_B had been large enough the pulse from A would already have been detected). At $t = \Gamma_A$ [Fig. 6(d)], the arrival of the leading edge of the primary pulse from A is recorded, and then at $t = \text{collision}$ [Fig. 6(e)] the collision starts after the pulse from A has already passed the detector. Finally at $t = \Gamma_B$ [Fig. 6(f)] the detector records the arrival time of the pulse from B.

In the next section when the data is presented, we will present measurements of the arrival time of the pulses from A following a collision, $\Gamma_{A,\text{collision}}$, and compare them to the arrival time when only driver A is triggered (driver B off, i.e., no collision), $\Gamma_{A,\text{direct}}$. For this case, $\delta_A < \delta_B$, no collision-induced effect is expected because the pulse from driver A does not collide until after it has been detected.

The schematic drawing for the case of $\delta_B < \delta_A$ is shown in Fig. 7. The order of the events is now reversed. At $t = \delta_B$ [Fig. 7(b)] the pulse from B is created and travels toward the detector. After the pulse from A is created [Fig. 7(c)] and the pulse from B is detected [Fig. 7(d)], the collision between the pulse from A and the pulse from B occurs [Fig. 7(e)]. Finally,

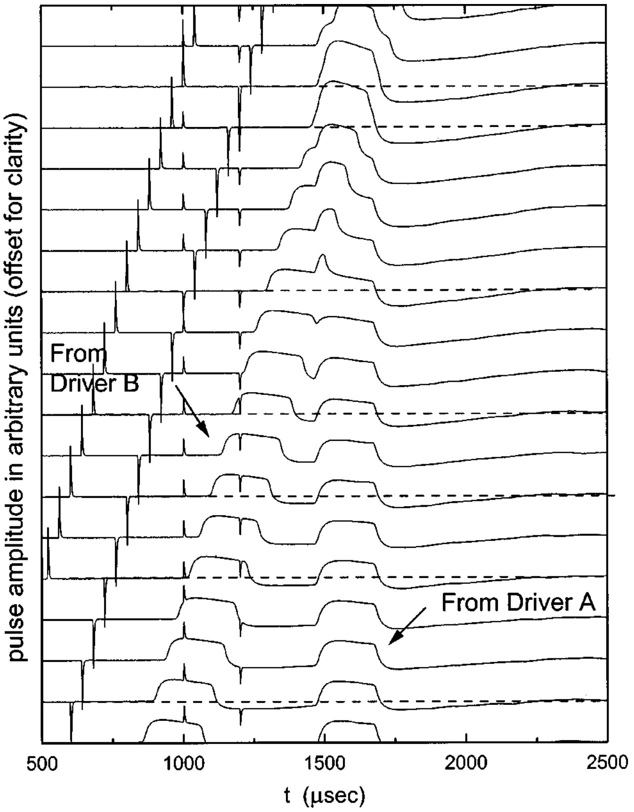

FIG. 10. Similar to the previous figure, this is an expanded waterfall plot of a collision event (shown in Fig. 8) with $W = 200\,\mu\text{sec}$ and $V^2 = 0.3\,(\text{volts})^2$ at $T = 1.453\,\text{K}$ and $d = 5.9$ layers. The change in the delay of the pulse from B from one data set to the next is 40 μsec. Here we examine a set of data with smaller values of δ_B to compare the size of the undershoot.

at $t = \Gamma_A$, the leading edge of the pulse from A arrives at the detector *after* having been involved in a collision. As we will see shortly, comparing $\Gamma_{A,\text{collision}}$ to $\Gamma_{A,\text{direct}}$ for the $\delta_B < \delta_A$ case shows that there is a shift in the arrival time due to the collision. This happens because during the collision the pulse from driver A resides on a film distorted due to the presence of the pulse from driver B. By varying δ_B we are able to study the complete evolution of pulse collisions and by adjusting δ_B so that the collision occurs in the vicinity of the detector we can observe directly the amplitude evolution during a collision event.

B. Third-sound collision amplitudes

We begin the examination of third-sound pulse collisions with some qualitative observations: we simply look at the pulse shapes that are present in collision events. As an example (others appear in Appendix B), we describe a series of such collisions where $\delta_A = 1000\,\mu\text{sec}$ (fixed) and $0 \leqslant \delta_B \leqslant 2000\,\mu\text{sec}$ and where δ_B was increased incrementally with an increment step size of 40 μsec through the range $0 \leqslant \delta_B \leqslant 2000\,\mu\text{sec}$. In each case the pulses from drivers A and B were of (unsaturated) amplitude 0.3 V^2 and width 200 μsec. The entire collection of collision data for this series of measurements is shown in Fig. 8 by vertically offsetting the data for each δ_B value so that the individual data sets can be examined. The pulse with an arrival time of $t = 1473\,\mu\text{sec}$ is the pulse from driver A for each A, B pulse pair for which we monitored the arrival time; i.e. δ_A was fixed. A closer examination of the third sound collision region for this data set is shown in Fig. 9. From a qualitative examination of the data, a number of the features generally attributed to third sound but not seen previously can be observed. As is clear from this figure, as the delay for the creation of the pulse from driver B, δ_B, is increased and the collision site is moved across the thermometer, the collision process is seen to involve amplitude addition as expected for wavelike phenomena. These pulses are of equal amplitude and the thermometer is located midway between the two sources. Thus, attenuation effects are equal for the two pulses. The incoming pulses, represented by the amplitude of the pulse from driver B in the data set denoted by the X is quantitatively half of the amplitude measured for the pulse represented by the data set Y for the case when the two pulses are superimposed. This is as one might expect for well-behaved waves. A similar addition takes place for the undershoot that follows each primary third-sound pulse. For example, as seen in Fig. 10 when the amplitude of the third-sound pulse is larger, the undershoot is larger (e.g., examine the size of the undershoot for an isolated pulse at the bottom of Fig. 10 and compare it

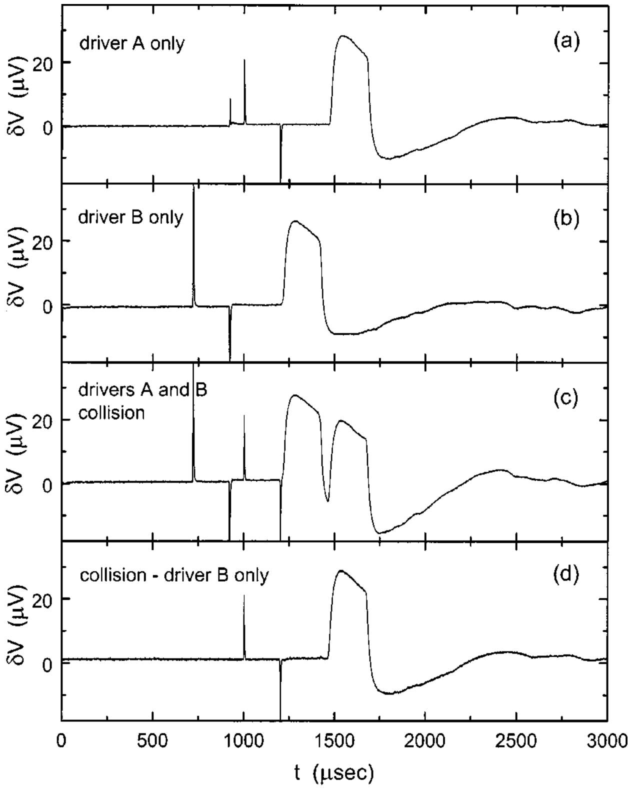

FIG. 11. Third-sound collision traces for $T = 1.453\,\text{K}$ and $d = 5.9$ layers. The trace in (a) is the pulse from driver A with $W_A = 200\,\mu\text{sec}$, $\delta_A = 1000\mu\text{sec}$ and $V_A^2 = 0.3\,(\text{volts})^2$. The trace in (b) is the pulse from driver B with $W_B = 200\,\mu\text{sec}$, $\delta_B = 720\,\mu\text{sec}$ and $V_B^2 = 0.3\,(\text{volts})^2$. In (c), both drivers were on, and the pulse from driver A was recorded here after a collision. In (d), we extract this collided pulse by subtracting (b) from (c).

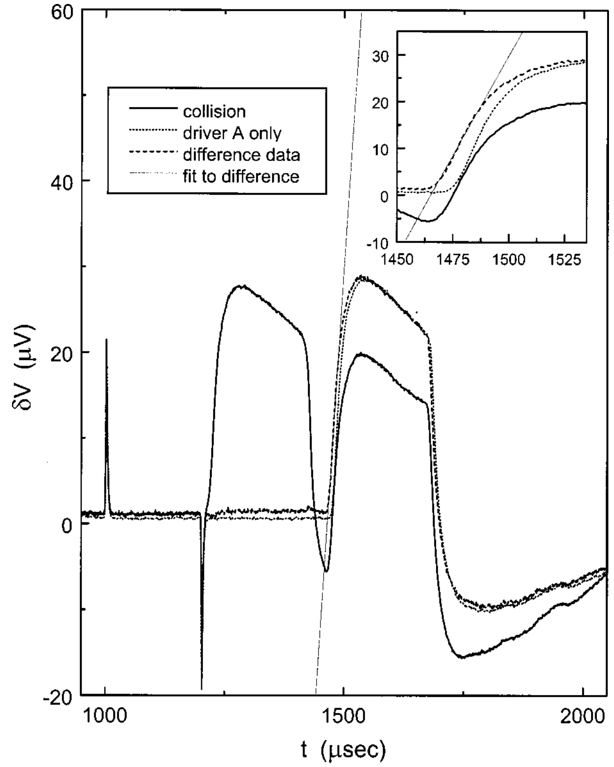

FIG. 12. Example of the calculation of the time of flight of the pulse from *A* after a collision occurred using the difference method. In the inset, the difference trace (dashed line) arrived before the direct trace (dotted line). To calculate the pulse arrival time, we used the technique described in the text.

with the size of the undershoot for the interaction pulses at the top of Fig. 10). In addition, a quantitative comparison between single pulses and the pulse marked *Y* in Fig. 9 shows that the superposition of the two third-sound pulses does not increase the width of the composite pulse.

To confirm that these effects are robust to changes in the drive amplitudes, widths, etc., we carried out a detailed study of various pulses in collision by varying a number of the relevant parameters. Some examples of the resulting collision events are shown in Appendix B.

C. Shift in arrival time

Having examined the amplitudes produced by third-sound collisions, we next turn to an examination of the arrival times of the pulses to see whether a third-sound pulse collision has an influence on the propagation time of the pulses. In Fig. 11, we show the results for a collision of third-sound pulses for a specific case for $\delta_B < \delta_A$. The drive pulse for each driver was $W = 200\,\mu$sec and $V^2 = 0.3\,(\mathrm{volts})^2$, but with different delay times ($\delta_A = 1000\,\mu$sec and $\delta_B = 720\,\mu$sec) causing the collision to occur between driver *A* and detector *D*2. These drive pulse amplitudes were small enough to ensure that the third-sound pulse amplitudes were midrange in the linear regime and were unsaturated (Fig. 5). The single pulses for drivers *A* and *B* are shown in Fig. 11(a) and Fig. 11(b), respectively. From the pulse *A* (only) data set [Fig. 11(a)], $\Gamma_{A,\mathrm{direct}}$ was determined. The pickup pulse signatures for each drive pulse can be observed at $t = \delta$ and $t = \delta + W$. In the data set of Fig. 11(c), both drivers were activated and the pulses recorded. The first pulse to arrive, from driver *B*, arrived directly, but the second pulse, from driver *A*, was first involved in a collision with the pulse from driver *B* before reaching the detector. In order to measure the time of flight of the pulse from driver *A* after the collision, we remove the signature of the pulse from driver *B* by subtracting data set (b) from data set (c). The result of this subtraction is shown in Fig. 11(d) and is called the *difference* data set. From the difference data set, $\Gamma_{A,\mathrm{collision}}$ was determined.

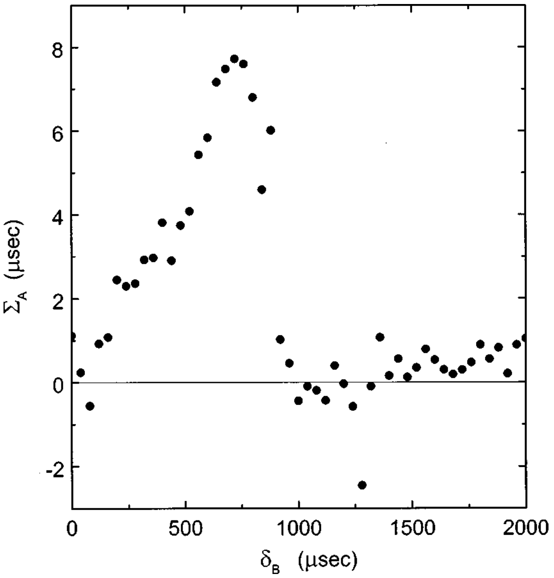

FIG. 13. Shift in the arrival time for third-sound pulses with $W_A = W_B = 200\,\mu$sec and $V_A^2 = V_B^2 = 0.3\,(\mathrm{volts})^2$ at $T = 1.453$ K and $d = 5.9$ layers as a function of δ_B.

For a closer view of the effect of the collision region, we show the collision data, the difference data and the data from driver *A* only in Fig. 12. The collision data is shown with the solid line. The dashed line represents the difference data (collision, *B* direct) and the dotted line is the data from driver *A* only. In the inset, we show the effect of the collision was to decrease the arrival time of the pulse involved in the collision (dashed line) with respect to the same initial pulse without a collision (dotted line). The arrival time, $\Gamma_{A,\mathrm{collision}}$ was found using the same technique outlined earlier using the difference data set. For these specific pulses, we found that the direct pulse arrived at $\Gamma_{A,\mathrm{direct}} = 1473.5\,\mu$sec and after a collision, the pulse arrived earlier at $\Gamma_{A,\mathrm{collision}} = 1465.8\,\mu$sec. The difference is defined as the shift, Σ_A, in the time of flight, $\Sigma_A = \Gamma_{A,\mathrm{direct}} - \Gamma_{A,\mathrm{collision}} = 7.7\,\mu$sec.

To repeat, for each pair of delays, (δ_A, δ_B), three data sets were recorded: driver *A* (only) activated, driver *B* (only) activated and both drivers activated (i.e., the collision data set). The arrival time in the collision data set, $\Gamma_{A,\mathrm{collision}}$ and the arrival time of the *A* (only) data set, $\Gamma_{A,\mathrm{direct}}$ were calculated using the difference method described earlier. The shift in the arrival time is defined by $\Sigma_A = \Gamma_{A,\mathrm{direct}} - \Gamma_{A,\mathrm{collision}}$, and the results for Σ_A for all of the data sets in Fig. 8 are shown in Fig. 13. Each different value of δ_B results in a data

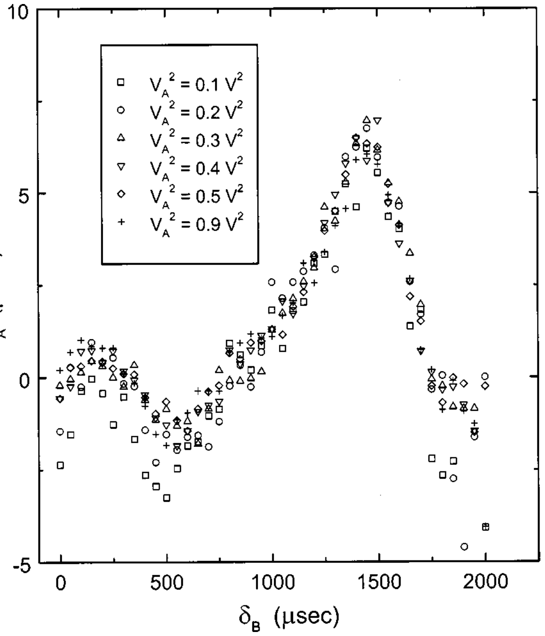

FIG. 14. Shift in the arrival time of the pulse from *A* due to a collision with a pulse from *B* at $T = 1.454$ K and $d = 5.9$ layers for various different amplitudes of driver *A*. For a range in amplitudes of *A*, the shape of the shift does not change. The shift in *A* did not depend on the amplitude of *A*. The pulse parameters here were $W_A = 200\,\mu$sec, $W_B = 300\,\mu$sec, $\delta_A = 1800\,\mu$sec, and $V_B^2 = 0.2$ (volts)^2.

point for Σ_A in Fig. 13. Obviously many such sets of data can be obtained by varying the several parameters available, and we will discuss these more extensive measurements in due course.

Even without a quantitative analysis, the general shape of the data shown in Fig. 13 can be understood qualitatively. Since the shift $\Sigma_A = \Gamma_{A,\mathrm{direct}} - \Gamma_{A,\mathrm{collision}} \geqslant 0\,\mu$sec, the effect of a collision was to reduce the arrival time of the pulse from driver *A*. For $\delta_B > \delta_A = 1000\,\mu$sec, the measured shift was 0 μsec. This is consistent with the discussion of the schematic diagram in Fig. 6 where the pulse from driver *A* arrived before colliding with the pulse from driver *B* and $\Sigma_A = 0\,\mu$sec is expected. At $\delta_B = \delta_A = 1000\,\mu$sec, the pulses arrive at the detector at the same time, but have not yet interacted. For the range $800\,\mu\mathrm{sec} \leqslant \delta_B \leqslant 1000\,\mu$sec, as δ_B decreases the pulse from driver *A* collides with more and more of the $W_B = 200\,\mu$sec wide pulse from *B* prior to arrival at the detector, and the shift increases to a maximum when the pulse from *A* collides with all of the primary pulse from *B*. Because even the unsaturated pulses used here were somewhat wider than the voltage step of the drive pulse, the largest shift occurred at $\delta_B \cong 720\,\mu$sec, i.e., about 280 μsec away from 1000 μsec (rather than 200 μsec). The magnitude of the largest shift, $\Sigma_{A,\max} = 7.7\,\mu$sec, is a ~1.7% change from $\tau_{A,\mathrm{direct}} = 473\,\mu$sec. For $\delta_B < 750\,\mu$sec, the pulse from *A* not only collides with all of the primary pulse from *B* (which tends to speed up the arrival of the pulse from driver *A*), but also some of the undershoot (which tends to slow down the pulse from driver *A*). The shift Σ_A therefore decreases in magnitude for $\delta_B < 720\,\mu$sec.

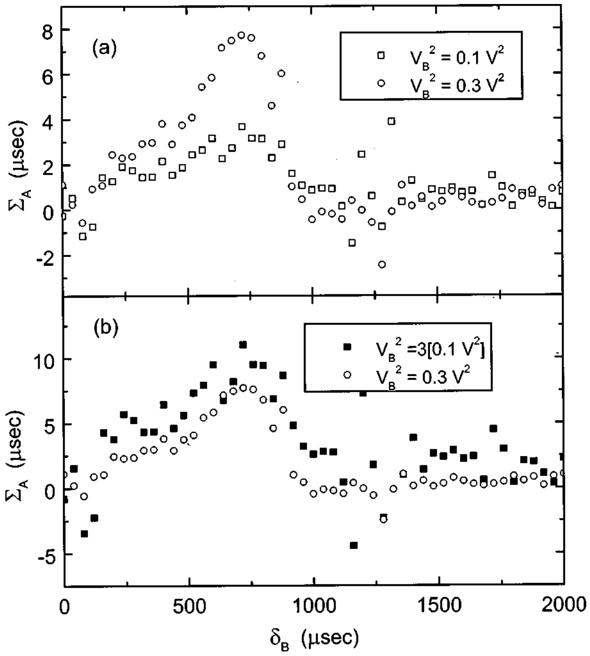

FIG. 15. (a) Shift in the arrival time of the pulse from *A* due to a collision with a pulse from *B* at $T = 1.453$ K and $d = 5.9$ layers for two different amplitudes of driver *B*. (b) $V_B^2 = 0.1\,V^2$ data from (a) multiplied by a factor of three (solid symbols).

We next determine which parameters influence the time of flight when a collision exists. In Fig. 14, we show the shift in the time of flight for a pulse from driver *A* for a range of amplitudes of driver *A*, a fixed width $W_A = 200\,\mu$sec, $W_B = 300\,\mu$sec, and fixed amplitude, $V_B^2 = 0.2$ (volts)^2, for driver *B*. The features are similar to Fig. 13. For $\delta_B > \delta_A = 1800\,\mu$sec, $\Sigma_A = 0\,\mu$sec. As the primary pulses collide, the shift increases, and then as *A* interacts with both the primary pulse and increasing amounts of the undershoot of the third-sound pulse from *B*, the shift decreases. Becuase we are only looking at the *arrival* time of the pulse from driver *A*, the shape of the shifts Σ_A does not depend on the amplitude of the pulse from driver *A*.

Changing the amplitude or width of the pulse from driver *B* results in a change in the shape of the shift curve. In Fig. 15(a) we show shifts for two different amplitudes from driver *B*. The pulse from driver *A* had parameters $W_A = 200\,\mu$sec, $V_A^2 = 0.3$ (volts)^2 and $\delta_A = 1000\,\mu$sec. The two types of pulses from driver *B* had a width $W_B = 200\,\mu$sec and amplitudes of 0.1 V^2 (squares) and 0.3 V^2 (circles). The magnitude of the shift due to the smaller drive amplitude case of pulse *B* is smaller, but the general shape of the curve is the same. When the size of the shifts for $V_B^2 = 0.1$ (volts)^2 is multiplied by a factor of three [Fig. 15(b)], the shifts more nearly agree, especially when the small systematic dc offset is ignored. This is not unexpected since the amplitude of a third sound pulse in the unsaturated regime is linearly proportional to V^2 and the velocity of third sound depends on the film thickness as $C \sim d^{-3/2}$. So, the amplitude of the pulse from driver *B* influences the arrival time of the pulse from driver *A*.

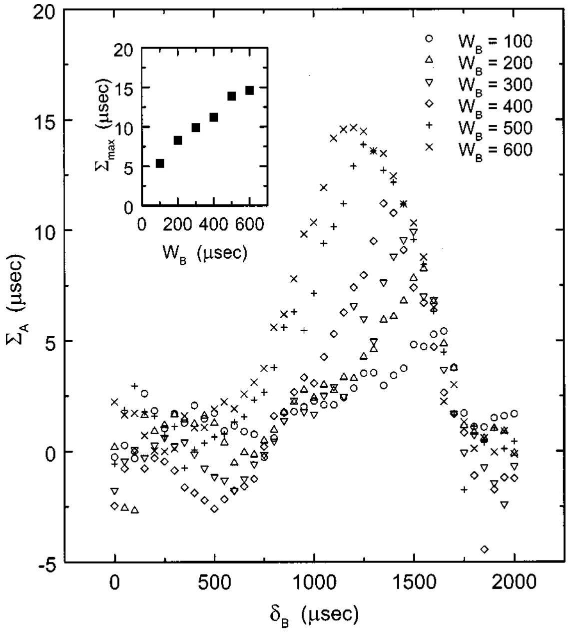

FIG. 16. Shift in the arrival time of the pulse from *A* due to a collision with a pulse from *B* at $T=1.454$ K and $d=5.5$ layers for six different widths (in μsec in the legend) of the pulse from driver *B*. In each case, $W_A=200\,\mu$sec, $V_A^2=0.3\,(\text{volts})^2$ and $V_B^2=0.3\,(\text{volts})^2$. The inset shows the maximum shift, $\Sigma_{\max}$, as a function of W_B.

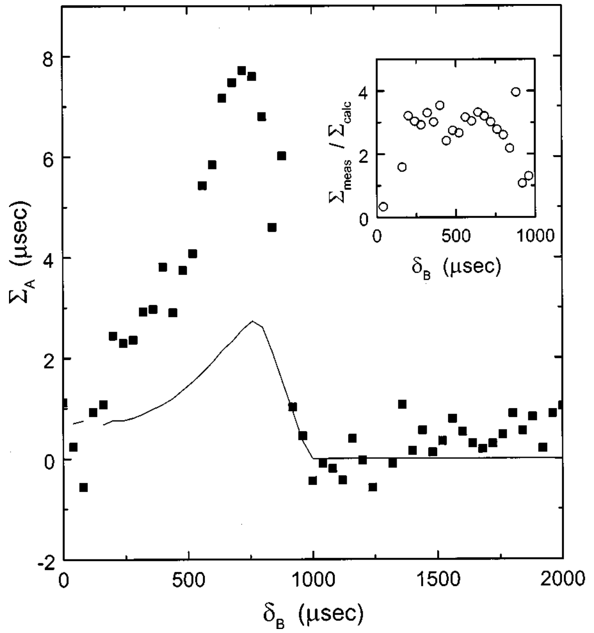

FIG. 17. Comparison of the measured shifts in the arrival time of a third-sound pulse after a collision to the calculated values found using the actual pulse shape. These shifts were at $T=1.453$ K and $d=5.9$ layers. In the inset, we show the ratio of the measured to the calculated shift.

Finally, we measured the size of Σ_A as a function of the width of the pulse from *B*. The results for six different values of $W_B 100 \leqslant W_B \leqslant 600\,\mu$sec are shown in Fig. 16 for the case of $\delta_A=1800\,\mu$sec. Increasing the width W_B increased $\Sigma_{A,\max}$ and shifted it to smaller values of δ_B. Notice in the individual data sets that in the time span from the maxima of Σ_A to $\delta_B=1800\,\mu$sec, the Σ_A traces all lie on top of one another. In this region, the pulse from driver *A* collides with the primary pulse from *B*. The longer it interacts with the primary pulse (i.e., the larger in width W_B is), the larger the shift. So, larger values of W_B produce larger values of $\Sigma_{\max}$ (inset, Fig. 16)

We have seen that the shifts in the arrival time of the pulse from *A* are increased by increasing the amplitude or width of the drive pulse at driver *B*, but not affected by the amplitude of the drive pulse at driver *A*. As alluded to earlier, one way to picture the collision generally is that the pulse from driver *B modifies* the properties of the film. Instead of a uniform thickness, the presence of the *B* primary pulse causes a local thin region and the presence of the *B* pulse undershoot causes a local thick region. When the pulse from driver *A* travels to the detector and collides with the pulse from driver *B*, it crosses these thin and thick regions, and when it does so its velocity changes accordingly. This causes the shift in the arrival time. In addition, local superfluid flow accompanies a propagating third sound pulse. This also influences the time of flight for one pulse that has collided with another.

D. Model prediction of the maximum shift

We can obtain a prediction for the size of the maximum shift, $\Sigma_{\max}$. During the collision, one pulse sees the other pulse as a modified film thickness. For example, decreasing the film thickness increases the third-sound velocity, which will decrease the arrival time of a pulse. In addition to a thickness change, third-sound pulses have local superfluid flow. This superfluid flow will also decrease the arrival time. For the moment, we simplify the collision process by assuming that the pulse of interest, from driver *A*, travels not on a uniform film, but on one which has a thin square-wave trough of width $W_B/2$. This thin trough is actually the pulse from driver *B* of width W_B and the factor of two arises from the fact that both pulses travel toward each other, decreasing the time interval during which the pulse from driver *A* rides on the pulse from driver *B* (for simplicity here we take the pulses from drivers *A* and *B* to have equal width). For the maximum shift, this trough is located immediately before the detector. The presence of the trough affects the pulse from driver *A* due to both a thinner film, $d-\delta d$, and a superfluid flow of magnitude v. Both of these effects work to cause the pulse from driver *A* to arrive at *D*2 earlier than a pulse from driver *A* on an undisturbed film (i.e., with no collision).

With the superfluid flow velocity and the film thickness change, we can predict the maximum shift, and then compare to the experimentally measured $\Sigma_{\max}\cong 8\,\mu$sec for the data presented in Fig. 13. Consider that at time $t=t_0$ an ideal square (symmetric) warm (thin) pulse travels across a substrate with equilibrium film thickness *d*, equilibrium temperature *T* and velocity C_3. At $t=t_0+dt$ the pulse advances a distance of $C_3 dt$. The advancing pulse displaces superfluid. The displacement process presumably occurs by means of a superfluid flow under the trough of the traveling pulse. If we assume a constant flow velocity that only exists under the trough, mass conservation leads to the relation

$$\langle \rho_s \rangle v_s dt\, l(d-\delta d) = \rho C_3 dt\, l\, \delta d, \tag{6}$$

where l is the width of the substrate. To first order, neglecting evaporation, condensation and substrate heating effects, the magnitude of the superfluid velocity under the pulse is

$$v_s = \left\langle \frac{\rho_s}{\rho} \right\rangle^{-1} C_3 \frac{\delta d}{d}. \tag{7}$$

The decrease in the time of flight, Σ_A, of the pulse from driver A due to this superfluid flow is given by the difference between the direct time of flight and the time of flight in the case of a collision. For a driver-detector separation of Δx,

$$\tau_{\mathrm{direct}} = \frac{\Delta x}{C_3(d)}. \tag{8}$$

When a collision occurs, the velocity changes for a portion of the trip. To first order, the distance over which the collision occurs is $C_3(d)W/2$ and the velocity of the pulse here will be $C_3(d-\delta d)+v_s$. The time of flight after a collision is

$$\tau_{\mathrm{collision}} = \frac{\Delta x - [C_3(d)W/2]}{C_3(d)} + \frac{[C_3(d)W/2]}{C_3(d-\delta d)+v_s}. \tag{9}$$

The total predicted shift due to the collision is then given by

$$\begin{aligned}\Sigma_{\mathrm{predicted}} &= \tau_{\mathrm{direct}} - \tau_{\mathrm{collision}} \\ &= \frac{W C_3(d)}{2}\left[\frac{1}{C_3(d)} - \frac{1}{C_3(d-\delta d)+v_s}\right].\end{aligned} \tag{10}$$

For thin films $(d \ll \beta)$, we can approximate the third-sound velocity by

$$C_3^2 = \left\langle \frac{\rho_s}{\rho} \right\rangle \left(1 + \frac{TS}{L}\right)^2 \frac{3\alpha}{d^3} \tag{11}$$

and reduce the equation for the predicted shift to the form

$$\Sigma_{\mathrm{predicted}} = \frac{W}{2}\left[\frac{1}{2}\left(3 - \frac{D}{d-D}\right) + \frac{\rho}{\rho_s}\frac{d}{d-D}\right]\frac{\delta d}{d}. \tag{12}$$

The first term is due to the change in thickness and the second term is due to the superfluid velocity field.

We calculate the predicted shift due to the combination of the film flow and the thinner film for the data shown in Fig. 13. These collisions occurred on a film with $T=1.453$ K and $d=5.9$ layers. From Fig. 12, the maximum amplitude of the difference pulse was $\delta V_{\mathrm{max}}=29\,\mu$V, which implies that $\delta T = 502\,\mu$K. This was the maximum temperature change, and from it we estimate the thickness change using Eq. (5). For the glass substrate, $\delta d = 121.2(\mathrm{layers/K})\delta T$, and the thickness amplitude of the third sound pulse was $\delta d = 0.061$ layers. For glass at $T=1.453$ K, the parameter $D=2.3$ layers and $\rho_s/\rho = 0.908$. From Eq. (12) and assuming the pulses are perfect troughs, we find that

$$\Sigma_{\mathrm{max,predicted}} = 3.4\,\mu\mathrm{sec}. \tag{13}$$

From the data in Fig. 13, the measured maximum shift was

$$\Sigma_{\mathrm{max,measured}} = 7.7\,\mu\mathrm{sec}. \tag{14}$$

This is reasonable agreement, but the maximum predicted shift for the ideal shaped pulses is smaller that the maximum measured shift by a little more than a factor of two.

The prediction for the size of the shift can be improved by using the actual measured pulse shape rather than assuming that the pulse is a perfect rectangular trough. This also allows us to extend the prediction to the entire third sound pulse rather than just predict the maximum shift due to the primary pulse. The pulse from driver B is broken into a number of adjacent ideal troughs and crests and using Eq. (12), each small thickness deviation's contribution to the total shift can be found, where in this case W is the width of one of the troughs or crests. The sum of all of the small contributions is then the total predicted shift.

We now use this procedure to calculate a predicted curve for the shifts reported in Fig. 13. The calculation results are shown as the solid line in Fig. 17 and the experimental results are shown as the symbols. The shape of the calculated shifts is similar to the measured shifts, but the values are smaller. In the inset, the ratio of the measured to the calculated shifts is shown to be about a constant factor of 3.

Next we examine the model to determine if the difference between the measured and predicted value of the shift is significant. First, we note that we measure the temperature amplitude of the third sound pulse, but the thickness amplitude is used in calculating the shifts. As pointed out earlier, Brooks *et al.*[17] measured both and found that $(\delta T/\delta d)_{\mathrm{measured}}$ was larger than $(\delta T/\delta d)_{\mathrm{calculated}}$. Incorporating this fact would decrease the predicted shift, not increase it.

Second, note in Fig. 13 the maximum shift occurred at $\delta_B = 720$. This suggests that even though the drive pulse was 200 μsec wide, the shift continued to increase after the primary pulse ended. We have made the assumption that the superfluid velocity flow decreases the arrival time only under the primary pulse. The calculation for the velocity, Eq. (7), suggests that the flow will change direction at the undershoot. If, after the primary pulse, the velocity flow is out of phase with δd the actual shift could continue to increase for a time during the undershoot. Given the simplicity of the model, the discrepancy between the predicted shift and the measured shift is perhaps not unreasonable, but it does appear that the discrepancy[27] is at least a factor of three, large enough to suggest something is missing in our understanding of third-sound pulse collisions.

V. CONCLUSIONS

We have reported measurements of single third-sound pulses and third-sound pulses in head-on collisions. An automated routine was used to find the time of flight of pulses generated at drivers A and B and received at detector $D2$. Knowledge of the distance between the drivers and detector allowed us to calculate the approximate film thickness from the third-sound velocity [Eq. (4)]. The saturation of amplitude for large amplitude third sound pulses was determined for 200 μsec pulses. For low drive powers, the pulse width was constant and the amplitude increased with increasing

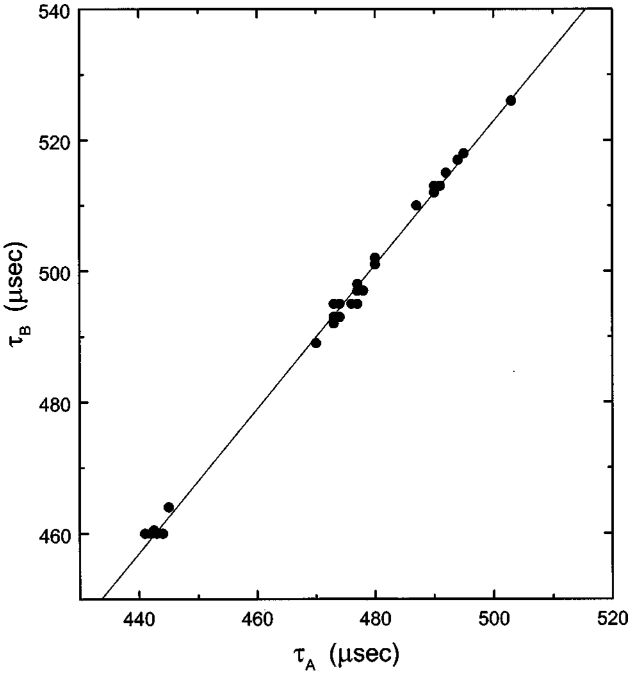

FIG. 18. Time of flight comparison for pulses arriving from driver *A* and driver *B*. The slope of the line, $m=1.10$, is not what was expected (see text).

drive power (linear region). Above the saturation threshold, $E_{\mathrm{sat}} \simeq 0.7\,\mu\mathrm{J}$ in Fig. 5, the pulse amplitude saturated and the width of the received pulse grew. These observations are consistent with earlier measurements.[11,23]

When both drivers were used at the same time, the features of head-on third-sound pulse collisions were studied. By delaying one square drive pulse relative to the other, the position of the collision on the substrate could be systematically changed. The amplitude of the third-sound pulse evolution during the collision process was studied and amplitude addition was observed. A collision decreases the arrival time of the collided pulse relative to the arrival time of the same pulse without the collision. For a range of relative delays, the measured shift in the arrival time as a function of the delay time was qualitatively explained. By considering the collision event as a single pulse riding on a film thickness fluctuation and superfluid flow (induced by the other pulse), we find that both features increase the velocity of the pulse. Quantitative comparison of the measured maximum arrival time shift with model-based predictions for primary pulse collisions provides only qualitative agreement with expectations.

ACKNOWLEDGMENTS

This work was supported by the National Science Foundation through Grants Nos. DMR 94-22208, DMR 97-29805, and DMR 98-19122 and by Research Trust Funds provided by the University of Massachusetts Amherst.

APPENDIX A

To further study this difference between the arrival times, we collected all of the τ_A and τ_B values for the recorded third-sound pulses in the collision experiment, and compare them revealing a nearly perfect linear dependence, Fig. 18. A linear fit to the (τ_A, τ_B) data results in $\tau_B = 1.0986\tau_A - 26.4\,\mu\mathrm{sec}$. If the third sound velocity were constant across the glass sample, the times of flight of the pulses would be related by the ratio of the distances, $\tau_B = \tau_A(\Delta x_B/\Delta x_A)$. The slope would be $\Delta x_B/\Delta x_A$ and the *y*-intercept would be 0. From the measurements, $\Delta x_B/\Delta x_A = 0.990$, different from the measured slope of 1.0986. The measurements of Δx_A and Δx_B include an uncertainty of 0.005 cm, not enough to account for the difference in the arrival times observed. These distances were measured from the inside edge of the driver to the inside edge of the detector. Since the strips have a width of 0.012 cm and different parts of the strip may have been more or less sensitive, the worst case measurement for the ratio would be for the case where the edge of the detector closest to *A* was most sensitive, and the close edge of driver *A* generated the pulse and the far edge of driver *B* created the pulse. In this case, $\Delta x_B/\Delta x_A = (0.998 + 0.012 + 0.012)/1.008 = 1.014$, still not consistent with the measured slope of 1.0986.

If the third-sound velocity was not constant on the glass slide, the gradient in the velocity could have been caused by either a persistent superfluid flow field or perhaps by asym-

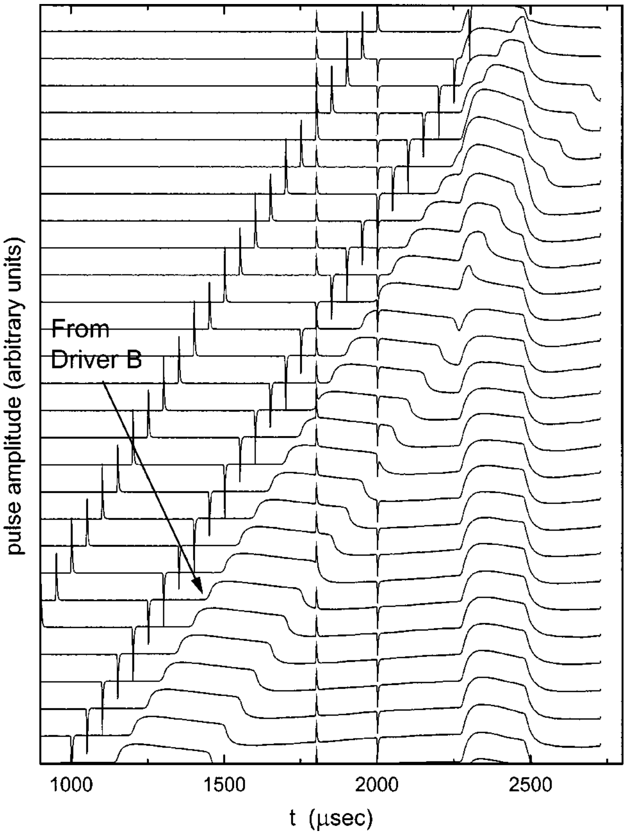

FIG. 19. An expanded waterfall plot of a collision event with $W_A = 200\,\mu\mathrm{sec}$ and $V_A^2 = 0.3\,(\mathrm{volts})^2$ and $W_B = 300\,\mu\mathrm{sec}$ and $V_B^2 = 0.2\,(\mathrm{volts})^2$ at $T = 1.453\,\mathrm{K}$ and $d = 5.84$ layers. The change in the delay of the pulse from driver *B* from one data set to the next is 40 μsec.

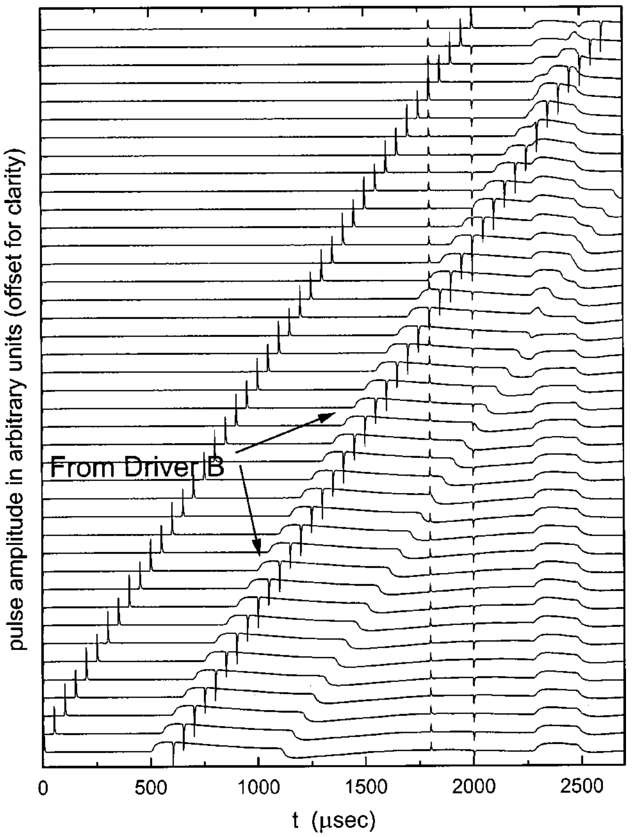

FIG. 20. An expanded waterfall plot of a collision event that involves third-sound pulses created in the nonsaturated regime with very different pulse widths. Here $W_A = 200\,\mu\text{sec}$ and $V_A^2 = 0.10\,(\text{volts})^2$ and $W_B = 600\,\mu\text{sec}$ and $V_B^2 = 0.15\,(\text{volts})^2$ at $T = 1.454\,\text{K}$ and $d = 5.9$ layers. The change in the delay of the pulse from driver B from one data set to the next is 40 μsec.

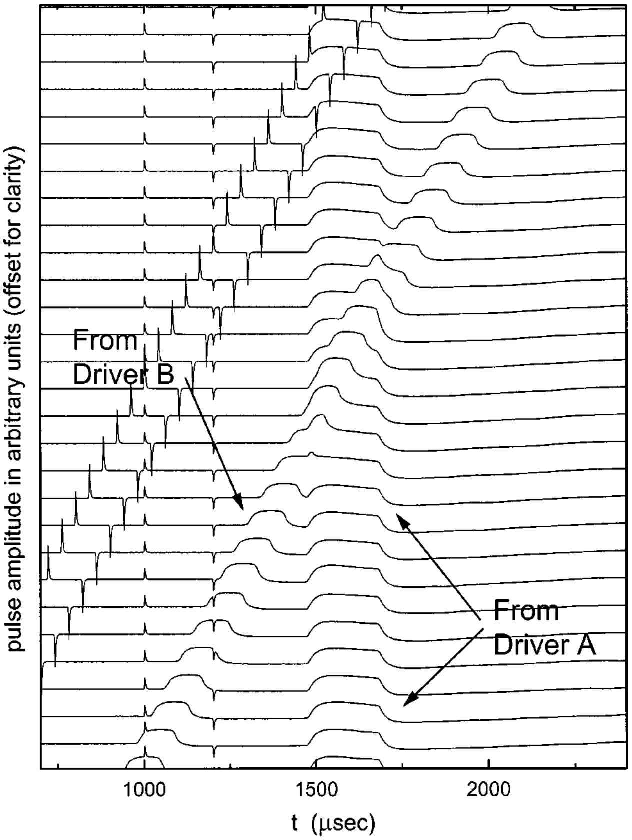

FIG. 21. An expanded waterfall plot of a collision event that involves third-sound pulses created in the nonsaturated regime. Here $W_A = 200\,\mu\text{sec}$ and $V_A^2 = 0.3\,(\text{volts})^2$ and $W_B = 100\,\mu\text{sec}$ and $V_B^2 = 0.3\,(\text{volts})^2$ at $T = 1.453\,\text{K}$ and $d = 5.9$ layers. The change in the delay of the pulse from driver B from one data set to the next is 40 μsec.

metric roughness on the surface of the glass slide. If a constant superfluid flow from A to B of magnitude v existed on the slide, the times of flight would be $\tau_A = \Delta x_A/(C_3 + v)$ and $\tau_B = \Delta x_B/(C_3 - v)$. Combining these equations,

$$\tau_B = \tau_A \frac{\Delta x_B}{\Delta x_A} - 2v. \tag{A1}$$

In this case, a nonzero intercept of $2v$ would be expected (observed in the data), but the slope is still predicted to be $\Delta x_B/\Delta x_A$.

APPENDIX B

In this appendix we show more examples of the behavior of the third-sound amplitude during a collision event. We vary some of the parameters of third-sound pulse creation and examine the effect that these changes have on the collision events.

In Fig. 19 pulses with different widths and amplitudes are shown ($V_A^2 = 0.3V^2$, $W_A = 200\,\mu\text{sec}$, $V_B^2 = 0.2V^2$, $W_B = 300\,\mu$ sec) and a quantitative examination of the amplitude behavior confirms that the composite pulse matches expectations based on amplitude addition. This and the data shown in the main text were for third sound pulses in the linear regime at creation (i.e., pulses that were not saturated in amplitude). As a second example, we show in Fig. 20 pulses of substantially different width ($W_A = 200$, $W_B = 600\,\mu$ sec) and different non-amplitude-saturated drives ($V_A^2 = 0.1V^2$, $V_B^2 = 0.15V^2$). As a similar example, we show in Fig. 21 waterfall plot with ($W_A = 200$, $W_B = 100\,\mu$ sec) and different non-amplitude-saturated drives ($V_A^2 = 0.3V^2$, $V_B^2 = 0.3V^2$). Behavior similar to that seen in the previous figures is apparent. For a third example (Fig. 22) we show an example for pulses so narrow ($W_A = W_B = 40\,\mu\text{sec}$) that they never reach a plateau amplitude[11] (i.e., had they a larger width, they would have achieved a larger amplitude for the drive voltage used). Behavior consistent with the other observations is seen. As a final example, we consider two third sound pulses initially created with a drive amplitude that is twice the threshold for third sound pulse saturation ($V_A^2 = V_B^2 = 1.0V^2$, $W_A = W_B = 200\,\mu$ sec). This drive results in a third-sound pulse wider than the drive voltage pulse and the result of a collision sequence is shown in Fig. 23. Since each pulse is saturated at the driver, each represents the largest such pulse amplitude that can be delivered to the thermometer by a single driver. But, the composite pulse at the thermometer is

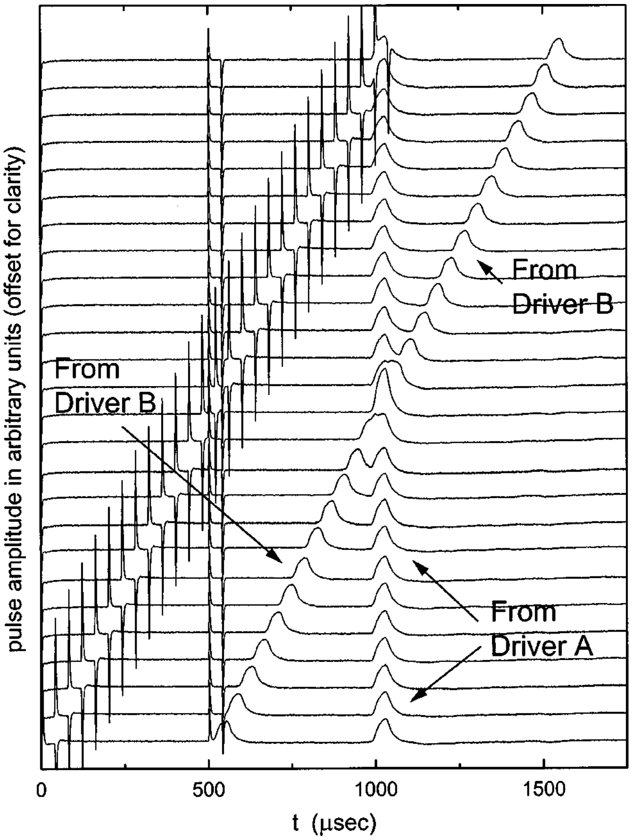

FIG. 22. An expanded waterfall plot of a collision event that involves third-sound pulses created in the nonsaturated regime of very small pulse width. Here $W_A = 40\,\mu$sec and $V_A^2 = 0.1\,(\text{volts})^2$ and $W_B = 40\,\mu$sec and $V_B^2 = 0.1\,(\text{volts})^2$ at $T = 1.453$ K and $d = 6.0$ layers. The change in the delay of the pulse from driver *B* from one data set to the next is 40 μsec.

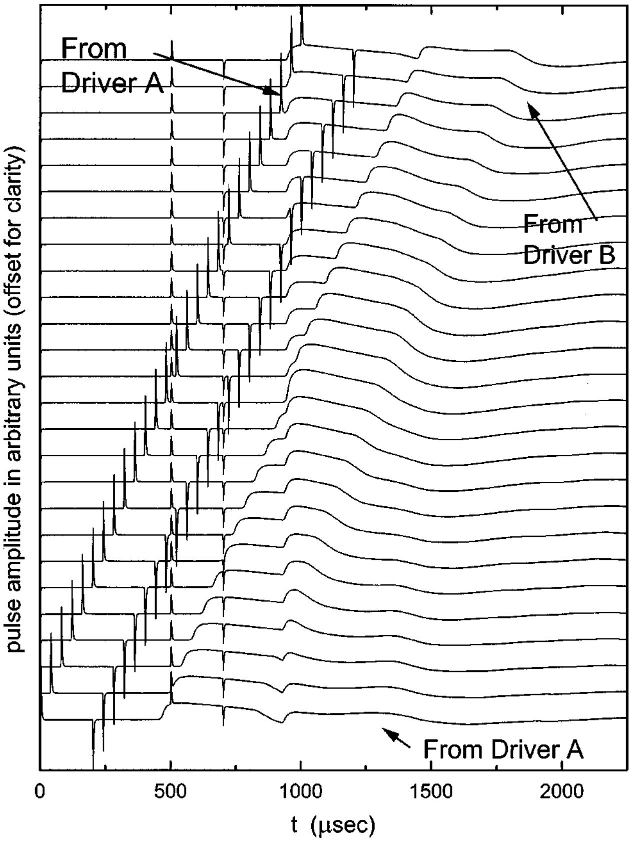

FIG. 23. Similar to the previous figures, this is an expanded waterfall plot of a collision event that involves third-sound pulses created in the saturated regime. Here $W_A = 200\,\mu$sec and $V_A^2 = 1.0\,(\text{volts})^2$ and $W_B = 200\,\mu$sec and $V_B^2 = 1.0\,(\text{volts})^2$ at $T = 1.460$ K and $d = 5.5$ layers. The change in the delay of the pulse from *B* from one data set to the next is 40 μsec.

larger in amplitude than the received individual saturated-at-creation pulses. This indicates that the technique of pulse collisions represents a technique by which a larger third-sound pulse can be delivered to a desired location on a substrate than any pulse that could be delivered by a single drive acting alone at an equal distance from the thermometer. This brings up the the possibility of producing enhanced-amplitude pulses by collision, pulses free from extraneous (e.g., broadening) effects produced by the pulse generation process. We did not fully explore such possibilities in this set of experiments. To do so will require a modified substrate design and attention to attenuation effects.

---

*Present address: Sandia National Laboratories, Albuquerque, NM.

†Present address: l'Ecole Normale Superiere, Paris, France.

[1] K. R. Atkins, Phys. Rev. **113**, 962 (1959).

[2] C. W. F. Everitt, K. R. Atkins, and A. Denenstein, Phys. Rev. Lett. **8**, 161 (1962); Phys. Rev. **136**, A1494 (1964).

[3] J. S. Brooks, F. M. Ellis, and R. B. Hallock, Phys. Rev. Lett. **40**, 240 (1978).

[4] I. Rudnick and J. C. Frasier, J. Low Temp. Phys. **3**, 225 (1970); J. H. Scholtz, E. O. McLean, and I. Rudnick, Phys. Rev. Lett. **32**, 147 (1974); **32**, 569(E) (1974).

[5] K. R. Atkins and I. Rudnik, *Progress in Low Temperature Physics*, edited by C. J. Gorter (North-Holland, Amsterdam, 1970), Vol. VI.

[6] D. Bergman, Phys. Rev. **188**, 370 (1969); D. J. Bergman, Phys. Rev. A **3**, 2058 (1971).

[7] I. Rudnick, Phys. Rev. Lett. **40**, 1454 (1978).

[8] J. Maps and R. B. Hallock, Phys. Rev. B **28**, 4021 (1983).

[9] K. L. Telschow and R. B. Hallock, Phys. Rev. Lett. **37**, 1484 (1976); Phys. Rev. B **27**, 3068 (1983); D. T. Ekholm and R. B. Hallock, Phys. Rev. Lett. **42**, 449 (1979).

[10] M. J. McKenna, R. J. Stanley, E. Dimasi, and J. D. Maynard, Physica B **165–166**, 603 (1990).

[11] S. Wang, K. S. Ketola, P. Lemaire, and R. B. Hallock, J. Low Temp. Phys. **119**, 645 (2000).

[12] D. T. Smith, C. P. Lorenson, R. B. Hallock, K. R. McCall, and R. A. Guyer, Phys. Rev. Lett. **61**, 1286 (1988); D. T. Smith, C. P. Lorenson, and R. B. Hallock, Phys. Rev. B **40**, 6634 (1989); **40**, 6648 (1989).

[13] The impedance of the continuous fill line for the 1 K pot consisted of 97 cm of 0.004 in. I.D. CuNi capillary with a measured impedance of $Z = 2.3 \times 10^{11}$ cm^3.

[14] The shifting procedure integrated the area, A, under a region of the data between the pickup signal and the arrival of the primary pulse, $t_{\mathrm{start}} \leqslant t \leqslant t_{\mathrm{end}}$, and the shifted trace was calculated using $\delta V(t) = V(t) - A/(t_{\mathrm{end}} - t_{\mathrm{start}})$. This served to normalize the data sets to a $\delta V(t) = 0$ baseline.

[15] S. J. Putterman, in *Superfluid Hydrodynamics*, edited by C. J. Gorter (North-Holland, Amsterdam, 1974), pp. 219–221.

[16] R. Galkiewicz, K. L. Telschow, and R. B. Hallock, J. Low Temp. Phys. **26**, 147 (1977).

[17] J. S. Brooks, F. M. Ellis, and R. B. Hallock, Phys. Rev. Lett. **40**, 240 (1978).

[18] F. M. Ellis, J. S. Brooks, and R. B. Hallock, J. Low Temp. Phys. **56**, 69 (1984).

[19] J. P. Laheurte, J. C. Noiray, J. P. Romagnan, and G. Rouille, Physica B **169**, 549 (1991); Phys. Rev. B **43**, 12837 (1991).

[20] It also should be noted that the experimental tests of the Bergman prediction for δT vs δd have all been carried out in a waveguide geometry and no measurements in a fully open geometry such as that used here have been done.

[21] J. P. Romagnan, J. C. Noiray, and J. P. Laheurte, J. Low Temp. Phys. **113**, 43 (1999) have found that the temperature of the film and that of a superconducting transition-edge thermometer may not be the same. This becomes a problem at low temperatures (e.g., below 1 K), but is not expected to be a problem at the temperatures used in this work. Since we will be primarily interested in pulse shapes and times of flight, this problem is of no consequence to us in any case.

[22] This definition differs from that used in our recent work[11] in a minor way, but this introduces no ambiguity or difficulty.

[23] K. S. Ketola, S. Wang, and R. B. Hallock, Physica B **194–196**, 649 (1994).

[24] K. S. Ketola, S. Wang, and R. B. Hallock, Physica B **194–196**, 653 (1994).

[25] M. P. Lilly, F. Portier, and R. B. Hallock, [LT-21], Czech. J. Phys. **46**, Suppl. S1, 423 (1996).

[26] For this work the typical third-sound velocity was ~2000 cm/sec. With a separation between a third-sound driver and a detector $(D2) \sim 1$ cm and a third-sound pulse width of typically ≈200 μsec, the third-sound pulses had a spatial extent of ≈0.4 cm. This is to be compared with the width of the third-sound drivers and detector (0.013 cm) and the separation between the drivers and the detector $D2(\sim 1$ cm$)$.

[27] One might take the modest systematic amplitude-dependent arrival time shifts for independent pulses discussed earlier in the text at face value. For pulses driven at amplitude 0.3 V^2 for the duration of the collision one might imagine that one has a pulse akin to one driven at 0.6 V^2. Taking into account the various relevant details shows that this effect, if present, would introduce <1 μsec shift, inadequate to explain the observations.